

Scalable 3D Gaussian Splatting-Based RF Signal Spatial Propagation Modeling

Kang Yang*
University of California, Los Angeles
Los Angeles, California, USA
kyang73@g.ucla.edu

Gaofeng Dong
University of California, Los Angeles
Los Angeles, California, USA
gfdong@g.ucla.edu

Sijie Ji
University of California, Los Angeles
Los Angeles, California, USA
California Institute of Technology
Pasadena, California, USA
sijieji@caltech.edu

Wan Du[†]
University of California, Merced
Merced, California, USA
wdu3@ucmerced.edu

Mani Srivastava[‡]
University of California, Los Angeles
and Amazon
Los Angeles, California, USA
mbs@ucla.edu

Abstract

Effective network planning and sensing in wireless networks require resource-intensive site surveys for data collection. An alternative is Radio-Frequency (RF) signal spatial propagation modeling, which computes received signals given transceiver positions in a scene (*e.g.*, a conference room). We identify a fundamental trade-off between scalability and fidelity in the state-of-the-art method. To address this issue, we explore leveraging 3D Gaussian Splatting (3DGS), an advanced technique for the image synthesis of 3D scenes in real-time from arbitrary camera poses. By integrating domain-specific insights, we design three components for adapting 3DGS to the RF domain, including Gaussian-based RF scene representation, gradient-guided RF attribute learning, and RF-customized CUDA for ray tracing. Building on them, we develop *RFSPM*, an end-to-end framework for scalable RF signal Spatial Propagation Modeling. We evaluate *RFSPM* in four field studies and two applications across RFID, BLE, LoRa, and 5G, covering diverse frequencies, antennas, signals, and scenes. The results show that *RFSPM* matches the fidelity of the state-of-the-art method while reducing data requirements, training GPU-hours, and inference latency by up to $9.8\times$, $18.6\times$, and $84.4\times$, respectively.

Keywords

RF Signal Spatial Propagation Modeling, Scalability

*This work was partially done when Kang Yang was a PhD student in Dr. Wan Du's group at UC Merced.

[†]Wan Du is the corresponding author.

[‡]Mani Srivastava holds concurrent appointments as a Professor of ECE and CS (joint) at the University of California, Los Angeles and as an Amazon Scholar. This paper describes work performed at the University of California, Los Angeles and is not associated with Amazon.

1 Introduction

Wireless networks, *e.g.*, WiFi and 5G, support both communication and sensing [1–3], but commonly encounter issues such as unreliable communication and insufficient training data. Reliable communication requires network planning to optimize transceiver placement using received signal data at various locations [4–7]. Similarly, sensing applications [8, 9], such as fingerprinting-based localization [10–12], rely on received signal data to train machine learning (ML) models. Site surveys [13], typically conducted to collect such data, are labor-intensive and time-consuming [14].

An alternative is RF signal spatial propagation modeling, which computes the received signal at a fixed receiver location given a transmitter emitting RF signals from any position in a scene. However, accurate modeling is challenging due to complex interactions between RF signals and objects like reflection, diffraction, and scattering [15–17]. Existing methods include simulations [18–20], empirical models [21–23], and ML models [24–26], but all suffer from low modeling fidelity due to notable limitations. Simulations require accurate scene priors, *e.g.*, Computer-Aided Design (CAD) models, which are rarely available. Empirical models oversimplify propagation with limited parameters, predicting only a single signal power. ML models map inputs to labels but fail to capture underlying propagation physics.

NeRF² [27] addresses these limitations by adapting Neural Radiance Field (NeRF) [28] to the RF domain, achieving state-of-the-art modeling fidelity. As depicted in Figure 1(a), the 3D space is divided into a dense grid of voxels. Each voxel has two attributes representing its impact on RF signal propagation: emission ψ and attenuation ρ . Attributes of each voxel are computed by querying a trained Multi-layer Perceptron (MLP) with input $\{x, y, z, \alpha, \beta, x_{tx}, y_{tx}, z_{tx}\}$. A ray tracing algorithm emits a ray γ from the receiver in

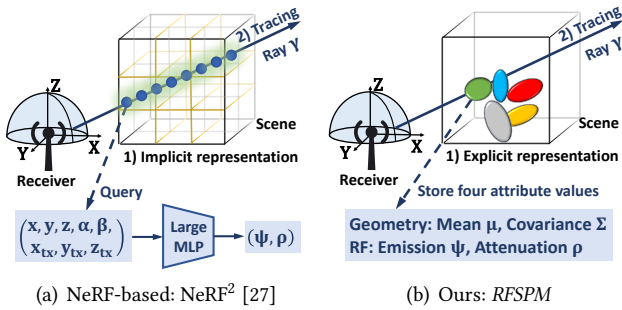


Figure 1: Both systems include scene representation & ray tracing. $\{x, y, z\}$: voxel position, $\{x_{tx}, y_{tx}, z_{tx}\}$: transmitter position, $\{\alpha, \beta\}$: azimuth and elevation of ray γ .

a direction $\{\alpha, \beta\}$, intersecting voxels along its path. The intersected voxels’ attributes are aggregated to compute the received signal in that direction. For hemispherical coverage, NeRF² emits 360×90 rays spanning directions ($360^\circ, 90^\circ$) at one-degree resolution. For a specific receiver location, an MLP is trained on signals received from various transmitter positions using mean squared error (MSE) loss.

However, NeRF²’s high modeling fidelity comes at the cost of extensive data, substantial training GPU-hours, and high inference latency, resulting in a scalability-fidelity trade-off (more experimental results in §4). *First*, the vast number of voxels (~ 31 million in a conference room) demands immense data to learn their attributes. *Second*, repeatedly querying the large MLP (~ 0.7 million parameters) during ray tracing is time- and computation-intensive.

This paper proposes *RFSPM*, a scalable RF signal spatial propagation modeling framework that matches NeRF²’s high fidelity while minimizing data requirements, GPU-hours, and inference latency, termed **S1- High Efficiency**. Furthermore, *RFSPM* offers two additional scalable features, addressing the limitations of conventional methods: **S2- Prior-Free**: Does not require scene priors, such as CAD models. **S3- Signal Versatility**: Supports diverse RF signal types, including signal strength, complex values, and spectrum.

Recently, in computer graphics, 3D Gaussian Splatting (3DGS) [29] is developed to enable real-time image synthesis for 3D scenes. 3DGS represents a scene as a collection of 3D Gaussian distributions. Each Gaussian has four attributes: mean (position), covariance matrix (defining size, shape, and orientation), color, and opacity. A pixel in an image is rendered by tracing a ray from the camera through the scene, intersecting 3D Gaussians along the ray. To identify which Gaussians the ray intersects, termed ray-Gaussian intersections, 3D Gaussians are projected (or “splatted”) onto the 2D image. The pixel value is computed by aggregating the color and opacity contributions from all the intersected Gaussians.

Inspired by 3DGS, *RFSPM* represents a scene using 3D Gaussian distributions to offer high efficiency. As illustrated in Figure 1(b), each Gaussian is parameterized by its mean μ and covariance Σ , which flexibly control its position, size, shape, and orientation. This flexibility enables a single Gaussian to efficiently encapsulate information that would otherwise require numerous voxels in NeRF²’s voxel grid representation. By adjusting the density of Gaussians, *RFSPM* assigns more Gaussians to regions with objects, while sparsely populating free spaces or homogeneous areas. Additionally, each Gaussian explicitly stores emission ψ and attenuation ρ , eliminating queries to large MLPs. The sparsity of Gaussians and direct attribute retention drastically reduce data requirements and ray tracing costs. However, transforming *RFSPM* into a practical system is challenging for three reasons.

C1- Directional and Phase Modeling: In 3DGS, a Gaussian’s color is parameterized by spherical harmonics (SH) coefficients [29, 30] to capture directional variations caused by optical effects such as reflections and shading. In contrast, RF signals with centimeter-scale wavelengths involve complex effects such as diffraction [15], along with phase impacts on constructive and destructive interference, none of which are well captured by SH coefficients [30, 31].

C2- Prior-Free Initialization: In 3DGS, the initialization of 3D Gaussians depends on a scene’s point cloud, which is generated using the Structure-from-Motion (SfM) algorithm [32] applied to input images. However, in the RF domain, no equivalent algorithm exists to derive a point cloud from RF measurements.

C3- Customized Ray Tracing: In 3DGS, ray tracing involves splatting, aggregation, and parallelization. Splatting relies on transformation matrices to project 3D Gaussians onto the 2D image plane, identifying ray-Gaussian intersections. Aggregation combines the color and opacity of intersected Gaussians to compute each pixel’s value. Since splatting requires traversing all Gaussians for each ray, 3DGS incorporates custom Compute Unified Device Architecture (CUDA) kernels [33] for efficient parallel GPU computation. However, in the RF domain, signals are received by antennas, lacking established transformation matrices for Gaussian splatting. Second, aggregation in RF signal modeling requires consideration of both amplitude and phase. Third, RF-specific splatting and aggregation computations necessitate redesigned CUDA kernels.

By tackling the three challenges above, we make the following three contributions.

i) Gaussian-Based RF Scene Representation: A scene is represented as customized 3D Gaussians. Each Gaussian is defined by four attributes: geometry-related, including the mean and covariance matrix; and RF-related, including emission and attenuation. Each Gaussian’s directional emission attribute is encoded by a dedicated small MLP instead of

SH coefficients. Additionally, RF-related attributes include amplitude and phase channels to capture phase information.

ii) Gradient-Guided Attribute Learning: Instead of initializing Gaussians with a point cloud or randomly, we partition the scene into equal-sized cubes and assign each cube’s center as a Gaussian’s mean. The covariance matrix is initialized based on the average distance to the three nearest cube centers, while attenuation and emission are assigned randomly. This cube-based strategy ensures that the initialized Gaussians cover the entire scene. All four Gaussian attributes are optimized using stochastic gradient descent (SGD) [34], with the number of Gaussians dynamically adjusted via a gradient-threshold-based mechanism.

iii) RF-Customized CUDA for Ray Tracing: Rays are emitted from the receiver in their respective directions. Ray-Gaussian intersections are identified through a proposed orthographic projection-based splatting module. A customized complex-valued blending algorithm aggregates RF-related attributes from the intersected Gaussians along each ray to compute the received signal. The computations for $360 * 90$ rays are parallelized using RF-customized CUDA kernels.

We evaluate *RFSPM* through three field studies and two applications (gateway coverage estimation and localization) across diverse frequency bands, antennas, signals, and scenes: RFID spatial spectrum synthesis [27], BLE and LoRa signal strength prediction. Results demonstrate that *RFSPM* matches the modeling fidelity of NeRF² [27] while delivering significantly higher efficiency. For instance, in RFID spatial spectrum synthesis, *RFSPM* matches NeRF²’s fidelity while reducing data requirements from 7.8 to 0.8 measurements/ft³, GPU-hours from 5.0 hours to 16.2 minutes, and inference time from 352.7 ms to 4.2 ms, achieving 9.8×, 18.6×, and 84.4× reductions, respectively.

These improvements offer substantial practical benefits. For example, localization tasks in a conference room ($26.2\text{ ft} \times 16.4\text{ ft} \times 9.8\text{ ft}$) [35], *RFSPM* can save up to 200 hours of data collection. With rapid training, it adapts to dynamic environments within minutes. Its low latency enables real-time applications like cellular downlink channel prediction, requiring inference within the 50 ms coherence time [25, 36].

2 Scenario Overview

We consider a scenario where a receiver is fixed at a position (e.g., 5G base station or LoRa gateway), while a transmitter (e.g., smartphone or LoRa node) can be at any location in 3D space. Given a dataset of some transmitter locations and their corresponding received signals, the goal is to predict the received signal from a transmitter at a new position.

Alternatively, the roles can be reversed: the transmitter is fixed (e.g., WiFi router), while the receiver is placed at different locations (e.g., smartphone). According to reciprocity

between the transmitter and receiver [25], these two scenarios are essentially equivalent. Consequently, this work focuses solely on the first scenario.

Received signal type depends on the receiver’s antenna setup. **i)** For an antenna array, the received signal is a $(360, 90)$ spatial spectrum matrix, where each entry represents the signal power in a specific direction at one-degree resolution. **ii)** For a single antenna, the received signal is either a single complex-valued measurement or a single signal power.

3 Related Work

i) NeRF-Based: NeRF² [27] develops voxel-based scene representations and ray tracing algorithms to achieve state-of-the-art modeling accuracy, outperforming conventional methods such as simulations [18–20], empirical models [21–23], and ML models [24–26]. However, it faces a scalability-fidelity tradeoff. *RFSPM* addresses this tradeoff through novel designs. *First*, *RFSPM* employs 3D Gaussians with varying positions, shapes, complex-valued emission and attenuation to construct a more flexible and expressive scene representation. This enables *RFSPM* to focus on object regions while avoiding large empty spaces. *Second*, each Gaussian explicitly stores its attributes, eliminating extensive large MLP queries. *Third*, the irregular and discrete placement of Gaussians renders voxel-based ray tracing ineffective. We address this with orthographic projection-based splatting to identify ray-Gaussian intersections, followed by a point-based complex-valued blending algorithm to aggregate emission, attenuation, and Gaussian shape contributions per ray.

NeWRF [37] shares the same methodology as NeRF² but differs in that it restricts rays to directions identified by Direction-of-Arrival (DoA) data, rather than considering all $360 * 90$ directions. However, collecting DoA data requires deploying an additional antenna array at each position, increasing the complexity and burden of data collection. This violates our three scalable principles. Consequently, we treat NeRF² and NeWRF as equivalent methods.

4 Scalability-Fidelity Tradeoff

This section presents a theoretical analysis of the inefficiencies of NeRF², followed by an empirical evaluation.

4.1 Theoretical Analysis

Two main factors cause the its low efficiency:

4.1.1 Vast Number of Voxels. The large number of voxels in a scene requires learning their attributes. For example, in a conference room $26.2\text{ ft} \times 16.4\text{ ft} \times 9.8\text{ ft}$ [35], with the voxel size set to $1/8$ of the wavelength (the default setting in NeRF² — 0.016 m for 2.4 GHz WiFi), there are approximately 31,257,628 voxels. Consequently, a large number of received

signals from diverse transmitter locations is required to cover as many of these voxels as possible.

4.1.2 Intensive Querying of Large MLPs. In NeRF², all voxels share a single MLP with a large number of parameters (e.g., 690,564) to capture variations among them. This large MLP introduces significant computational overhead. During ray tracing, each ray intersects multiple voxels, and the attributes of each voxel are computed by querying the MLP with input $\{x, y, z, \alpha, \beta, x_{tx}, y_{tx}, z_{tx}\}$. Repeatedly querying the MLP for numerous voxels introduces high computational costs, slowing down both training and inference.

4.2 Empirical Evaluation

We conduct experiments to evaluate the efficiency of NeRF² using the RFID spatial spectrum dataset described in Section 7.1. The dataset consists of 6,123 transmitter positions and their corresponding received spatial spectrum at a fixed receiver equipped with an antenna array.

4.2.1 Data Efficiency. Efficient models require less training data while maintaining accuracy [38–40]. Reducing training data simplifies data collection and accelerates deployment, enhancing scalability across various applications [41]. For example, in network planning, fewer training samples reduce the effort required to map the signal environment, enabling faster network setup and optimization [42].

Data density is defined as the total amount of training data divided by the volume of the 3D scene, measured in measurements/ft³. We set seven densities (0.8, 1.6, 3.1, 4.7, 7.8, 12.4, and 15.5) to train NeRF² separately and evaluate each trained model on the same testing dataset. The fidelity of the synthesized spectrum is assessed using the Peak Signal-to-Noise Ratio (PSNR) metric, as the spectrum can be viewed as an image (Figure 6). Figure 2 demonstrates that increasing measurement density improves the fidelity of the synthesized spectrum. When the measurement density reaches 12.4 or 15.5, the PSNR converges, indicating that a minimum density of 12.4 is required. This high data requirement is burdensome, making the data collection process resource-intensive.

4.2.2 Training GPU-hours. Efficient models would exhibit short training GPU-hours [43–45]. For example, in fingerprint-based localization tasks, rapid training of RF signal propagation models enables quick data synthesis for updating the fingerprint database. This allows the database to adapt swiftly to changes in layouts, furniture arrangements, or interference sources, thereby maintaining localization accuracy with minimal delays. Moreover, shorter training GPU-hours help conserve computational resources.

Figure 3 illustrates the training time required for NeRF² to converge using NVIDIA GeForce RTX 3080 Ti or 4090 GPUs. The average training time is 5.01 hours with a standard

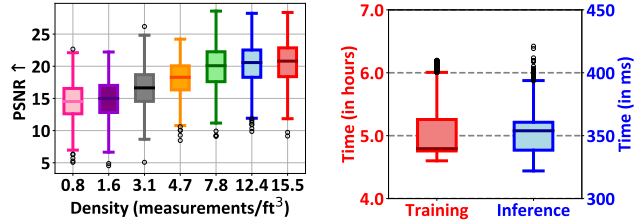


Figure 2: Training data efficiency of NeRF² [27]. **Figure 3: Training (hours) and inference times (ms).**

deviation of 0.38 hours, which is considerably long. These prolonged training times delay fingerprint database updates and demand substantial computational resources.

4.2.3 Inference Latency. Efficient models are characterized by low inference latency [46–48]. In real-time applications, such as channel prediction in 5G, inference latency must be shorter than the coherence time [25], which represents the interval over which the channel remains relatively constant [25]. The average inference latency of NeRF², depicted in Figure 3, is 352.73 ms. This far exceeds the coherence time of 50 ms for a moving transmitter [36].

5 Design of RFSPM

Figure 4 illustrates RFSPM, which synthesizes the received signal at a specific receiver for a transmitter positioned at any location in the scene. *i) Gaussian-based RF scene representation* models the scene with 3D Gaussians, each storing geometric and RF-related attributes. *ii) Gradient-guided attribute learning* optimizes these attributes via gradients while dynamically adjusting the number of Gaussians. *iii) RF-customized CUDA for ray tracing* computes the received signal by emitting rays from the receiver, identifying ray-Gaussian intersections via orthographic projection-based splatting, and aggregating RF attributes along each ray.

5.1 Gaussian-Based Scene Representation

Each customized 3D Gaussian distribution carries four attributes: *i) mean μ* and *ii) covariance matrix Σ* , which define its geometric properties, including position, size, shape, and orientation; *iii) emission ψ* and *iv) attenuation ρ* , which characterize the Gaussian’s influence on RF signal propagation.

i) Mean μ and ii) Covariance Matrix Σ : A 3D Gaussian distribution resembles an ellipsoid, representing a probability distribution in 3D space, as defined by the probability density function (PDF) in Equation (1). The center of the distribution is a 3D position (mean μ), indicating the peak location, while the spread and orientation in space are determined by a full 3×3 covariance matrix Σ :

$$P(\mathbf{x}) = e^{-\frac{1}{2}(\mathbf{x}-\mu)^T \Sigma^{-1}(\mathbf{x}-\mu)} \quad (1)$$

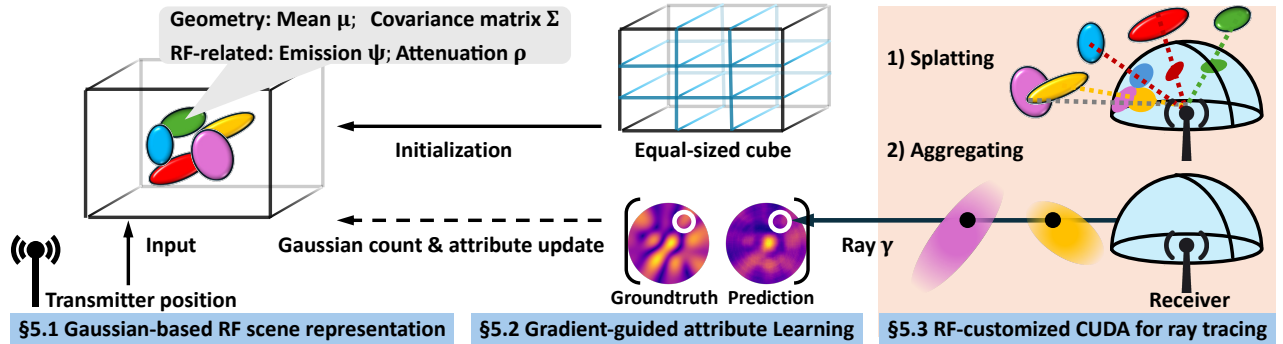


Figure 4: Illustration of the *RFSPM* architecture, trained end-to-end, consisting of three main building blocks.

iii) **Emission ψ** : Each point on a wavefront serves as a source of wavelets, according to the Huygens–Fresnel principle [49]. Analogously, when an RF signal from a transmitter encounters a 3D Gaussian, the Gaussian acts as a scattering point, re-emitting an RF signal termed emission ψ . This emission is characterized by $\psi = |\psi| e^{j\angle\psi}$, where $|\psi|$ represents the amplitude and $\angle\psi$ denotes the phase.

Emission ψ varies due to factors such as surface orientation relative to the incident signal and the material properties at the Gaussian’s position. Moreover, the transmitter position influences ψ by altering the incident angle. Thus, ψ depends on both the direction and the transmitter position. To this end, we employ a small neural network, f_{Θ} , within each Gaussian to encode the directional emission signal:

$$\psi = f_{\Theta}(x_{\text{tx}}, y_{\text{tx}}, z_{\text{tx}}, \alpha, \beta) \quad (2)$$

where f_{Θ} takes the transmitter position $\{x_{\text{tx}}, y_{\text{tx}}, z_{\text{tx}}\}$ and the direction $\{\alpha, \beta\}$ as inputs and outputs the corresponding emission ψ . Here, $\{\alpha, \beta\}$ represents the direction from the 3D Gaussian’s position to the receiver. Since f_{Θ} models only its own Gaussian’s emission, it has a small number of parameters, *i.e.*, two fully connected layers with ReLU activation.

iv) **Attenuation ρ** : An RF signal passing through a 3D Gaussian undergoes attenuation ρ , resulting in an amplitude reduction $|\rho|$ and a phase shift $\angle\rho$. According to Maxwell’s equations [17], attenuation depends on material properties. Thus, the attenuation ρ of a 3D Gaussian is primarily determined by the material properties at its location.

5.2 Gradient-Guided Attribute Learning

We initialize the number of Gaussians and their attributes, then optimize both with gradient-based strategies. Gradients are calculated after computing the loss in §5.4. Finally, we discuss the efficiency of using 3D Gaussians.

5.2.1 *Cube-Based Initialization*. We partition the scene into equal-sized cubes, each with a side length L_{cube} , empirically set to six times the wavelength. The center of each cube is assigned as a Gaussian’s mean. The covariance matrix is

initialized based on the average distance to the N_{cube} nearest cube centers, where N_{cube} is set to three, while attenuation and emission are assigned randomly. Compared to random initialization, this cube-based strategy ensures that the Gaussians cover the entire scene, leading to faster convergence.

5.2.2 *Gradient-Based Updating*. The following two strategies are employed to update the number of Gaussians and their attributes for flexible and efficient scene representation.

i) **Attribute Updating**: Each 3D Gaussian explicitly stores its own attributes and updates them using SGD [34]:

$$w^{(j+1)} = w^{(j)} - \eta_w \cdot \nabla_w \mathcal{L}(w^{(j)}) \quad (3)$$

where w represents any attribute of a Gaussian, each with its own learning rate η_w . The term $\nabla_w \mathcal{L}(w^{(j)})$ denotes the gradient of the loss function \mathcal{L} , defined in Equation (8), with respect to w at iteration j . For emission ψ , the updated parameters belong to the network f_{Θ} .

The covariance matrix Σ is physically meaningful only when positive semi-definite [50], but the update equation above does not guarantee this property. To address this, we adopt the solution proposed in [29], which represents Σ as $\Sigma = RSS^T R^T$, where R is a rotation matrix and S is a scaling matrix. Updates are applied independently to R and S , ensuring that Σ remains positive semi-definite.

ii) **Number of Gaussian Updating**: The initial number of Gaussians is set by cube-based initialization. However, this number is suboptimal, as some areas require more Gaussians (*e.g.*, object regions), while others need fewer (*e.g.*, free space) to model RF signal propagation effectively. We observe that such cases lead to large gradients for the Gaussian’s mean μ , as the existing 3D Gaussians do not adequately capture the area’s effect on RF signal propagation. The mean μ exhibits larger gradients than other attributes because it represents the position with the highest probability, making it crucial for modeling RF signal behavior.

To this end, we employ a gradient-threshold-based strategy: *First*, every N_{μ} iterations, we compute the average gradient of the mean μ for all Gaussians and select those with

a mean gradient exceeding a threshold ϵ_μ . *Second*, we determine the radius of each selected Gaussian, approximated as the average of the diagonal values of its covariance matrix. A radius threshold ϵ_r classifies them as small or large Gaussians. *Third*, small Gaussians are cloned by duplicating them and shifting the copies in the direction of the gradient. Large Gaussians are split into two new Gaussians, reducing their scaling matrix R by a factor of ϕ and initializing their positions by sampling from the original Gaussian’s PDF.

Additionally, every N_ρ iterations, we remove Gaussians with attenuation ρ below a threshold ϵ_ρ , as they minimally impact signal propagation, e.g., in free space. A single 3D Gaussian distribution can represent a large free space.

5.2.3 Efficiency of 3D Gaussian. Unlike fixed voxel grids, which require numerous voxels to capture the entire scene’s effects on signal propagation, 3D Gaussians adjust their position, shape, size, and orientation to represent these effects. This adaptability enables 3D Gaussians to achieve similar representation quality with far fewer voxels, improving computational efficiency and reducing training data requirements. For example, a typical conference room [35] requires learning the attributes of 31,257,628 voxels (Section 4.1). In contrast, only 393,920 Gaussians may be needed, an ~ 80 -fold reduction, assuming the optimal count matches the number of points in the conference room’s point cloud data.

5.3 RF-Customized CUDA for Ray Tracing

The emitted rays from the receiver are formalized, followed by an orthographic projection-based splatting module, which identifies Gaussians intersected by each ray. Next, the complex-valued blending algorithm computes the received signal based on these intersections. Finally, computation is parallelized using customized CUDA kernels.

5.3.1 Definition of Rays. Rays extend from the receiver in various directions, e.g., ray γ in Figure 5:

$$\gamma(d) = \mathbf{I}_{\text{rx}} + d\hat{\mathbf{v}}, \quad \text{where } d \geq r_{\text{rx}} \quad (4)$$

where d is the distance from the receiver to a point $r(d)$ on the ray, $\mathbf{I}_{\text{rx}} = (x_{\text{rx}}, y_{\text{rx}}, z_{\text{rx}})$ denotes the receiver position, and the unit vector $\hat{\mathbf{v}} = (\cos \alpha \cos \beta, \sin \alpha \cos \beta, \sin \beta)^\top$ defines the ray direction, with α and β as the azimuthal and elevation angles, respectively. The condition $d \geq r_{\text{rx}}$ indicates that the ray starts at a distance r_{rx} from the receiver. Thus, $360 * 90$ rays are emitted from a spherical surface centered at the receiver with radius r_{rx} . We refer to this surface as the Ray Emitting Spherical Surface (RESS).

5.3.2 Orthographic Projection-Based Splatting. The uniform voxel grid structure allows straightforward identification of the voxels a ray passes through. However, the irregular and discrete placement of 3D Gaussians complicates determining

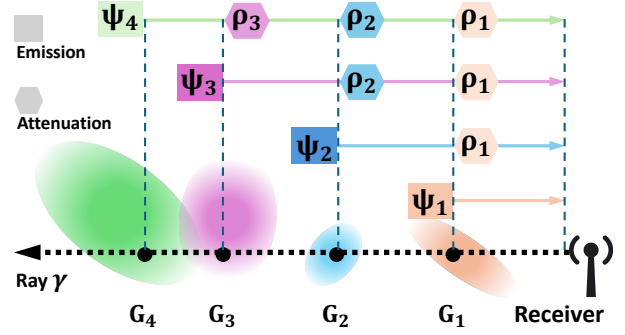


Figure 5: Illustration of the complex-valued blending algorithm, which calculate the received signal in direction γ . Four 3D Gaussians are shown, where ψ and ρ denote the emission and attenuation of each Gaussian. Each emission ψ_i is attenuated by ρ_m from Gaussians m (from 1 to $i - 1$). The final received signal in direction γ is the sum of these attenuated emissions.

which Gaussians a ray intersects. Intuitively, each ray must be checked against all Gaussians, resulting in a computational complexity of $O(M \times N)$, where M is the total number of rays and N is the total number of Gaussians.

In 3DGS, to accelerate the determination of which Gaussians affect each ray (pixel), 3D Gaussians are projected (or "splatted") onto a 2D image plane. This splatting process utilizes the View Matrix, Projection Matrix, and Jacobian Matrix [51] to form 2D Gaussians on the image plane. Each projected 2D Gaussian is represented as a circle centered at its mean, with a radius determined by the 2D covariance matrix. Pixels (rays) within this circle are considered affected by the original 3D Gaussian. This splatting reduces computational complexity to $O(N)$ by localizing each Gaussian’s influence to a specific region on the image plane.

2D RF Plane: The above splatting is not applicable in the RF domain without an image plane. Instead, the received signal is measured on the RESS. To enable splatting, the RESS is transformed into a 2D RF plane. Specifically, the Cartesian coordinates (x, y, z) of each point on the RESS are converted to spherical coordinates (ζ, α, β) , with (α, β) rounded to the nearest integers to achieve one-degree resolution:

$$\begin{pmatrix} \zeta \\ \alpha \\ \beta \end{pmatrix} = \begin{pmatrix} \sqrt{x^2 + y^2 + z^2} \\ \arctan 2(y, x) \\ \arccos\left(\frac{z}{\sqrt{x^2 + y^2 + z^2}}\right) \end{pmatrix} \quad (5)$$

$$x' = \lfloor \alpha \rfloor, \quad y' = \lfloor \beta \rfloor$$

where ζ is the radial distance, α the azimuthal angle, β the elevation angle, and $\lfloor \cdot \rfloor$ the floor function. (x', y') represents the projected coordinates in the 2D RF plane.

Splatting: Each 3D Gaussian is splatted onto the RF plane, forming a 2D Gaussian represented as a circle. Gaussian

mean μ is projected onto the 2D plane using Equation (5), defining the circle’s center. Jacobian matrix [51] maps the 3×3 covariance matrix into a 2×2 covariance matrix, whose eigenvalues determine the circle’s radius. Rays within this circle are considered influenced by the original 3D Gaussian.

5.3.3 Complex-Valued Blending Algorithm. We introduce a complex-valued blending algorithm to process a given ray and its identified intersected Gaussians. First, the Gaussians are sorted by their distance to the receiver. Then, the received signal for the ray is computed by aggregating their RF attributes, incorporating both amplitude and phase channels:

$$S = \sum_{i=1}^{N_{\text{intr}}} |\psi_i| e^{j\angle\psi_i} \cdot \prod_{m=1}^{i-1} (1 - |\rho_m| e^{j\angle\rho_m}) \quad (6)$$

where S is the received signal for a ray, N_{intr} denotes the number of Gaussians intersecting the ray, and ψ_i and ρ_m represent the emission and attenuation of the i -th and m -th Gaussians, respectively. Emission ψ_i is attenuated by ρ_m from preceding Gaussians. The received signal is the sum of these attenuated emissions. Figure 5 illustrates a ray intersecting four Gaussians, represented as follows:

$$S = \psi_1 + \psi_2 \cdot (1 - \rho_1) + \psi_3 \cdot (1 - \rho_2) \cdot (1 - \rho_1) + \psi_4 \cdot (1 - \rho_3) \cdot (1 - \rho_2) \cdot (1 - \rho_1) \quad (7)$$

Impact of Gaussian Geometry: In a voxel-based ray tracing algorithm, a ray is assumed to pass through the center of each voxel. However, this assumption does not hold in Gaussian-based scene representation. For example, in Figure 5, both G2 and G3 intersect the ray, but the intersection point on G2 is closer to its mean than that on G3. Even if G2 and G3 share the same emission and attenuation attributes, their contributions to the final received signal differ due to the varying distances of their intersection points from their means. These distances affect the probability of each Gaussian influencing the ray. Therefore, the blending process in Equation (6) should account for Gaussian geometry.

To achieve this, the intersection point is first determined by solving the ray equation (Equation 4) and the ellipsoid equation (Equation 1). If two solutions exist, their midpoint is taken as the intersection point. Next, the distance between the intersection point and the Gaussian’s mean is calculated. The intersection probability p_{intr} is then determined by evaluating the Gaussian’s PDF at this distance. Finally, the emission is adjusted by multiplying it by p_{intr} : $\psi = p_{\text{intr}} \cdot \psi$.

5.3.4 CUDA Kernel. We develop two CUDA kernels for the forward and backward computations in ray tracing.

Forward Kernel: Algorithm 1 outlines the forward kernel. The inputs include the number of rays in azimuth and elevation, the means, covariance matrices, emissions, and attenuations of all 3D Gaussians, as well as the positions

Algorithm 1: Forward CUDA Kernel for Ray Tracing

Input: w, h : numbers of rays in azimuth and elevation
Input: M, C : means & covariances of all Gaussians
Input: E, A : emissions & attenuations of all Gaussians
Input: L : positions of receiver and transmitter
Output: O : received signals for all rays

```

1 Function RayTracing( $w, h, M, C, E, A, L$ ):
2    $M', C' \leftarrow$  sphericalGaussian( $M, C, L$ )
3   Grids  $\leftarrow$  buildGrid( $w, h$ )
4   Idx, Kys  $\leftarrow$  sphericalSplatting( $M',$  Grids)
5   Ranges  $\leftarrow$  computeGridRange( $Idx,$  Kys)
6    $O \leftarrow 0$ 
7   forall grid  $G$  in Grids do
8     forall ray  $i$  in  $G$  do
9       ra  $\leftarrow$  getGridRange(Ranges,  $g$ )
10       $O[i] \leftarrow$  Blend( $i,$  Idx, ra Kys,  $M', C', E, A$ )
11    end
12  end
13  return  $O$ 

```

of the receiver and transmitter. The output is the received signal computed for all $360 * 90$ rays.

Specifically, Line 2 projects 3D Gaussians onto the 2D RF plane. Line 3 partitions all rays into multiple grids, each containing N_{rays} rays in the azimuth and elevation directions, to accelerate processing. Line 4 applies the splatting process to identify which Gaussians influence each grid. Line 5 records the sorted Gaussians within each grid. Finally, Lines 7–12 compute the received signal for each ray in parallel using the complex-valued blending algorithm.

Backward Kernel: Since the Forward Kernel is invoked for ray tracing forward computation, PyTorch cannot automatically compute the corresponding computation graph gradients. After computing the received signal S and the loss \mathcal{L} , PyTorch calculates the gradient $\frac{\partial \mathcal{L}}{\partial S}$, which is then passed to the Backward Kernel. This kernel reverses the computations of the Forward Kernel to compute the gradients for each Gaussian attribute.

5.4 Training Loss

After calculating the received signal for each ray, the choice of loss function depends on the type of receiver antenna.

i) Antenna Array: When the receiver is an antenna array, it captures signal power from all directions, represented as a $(360, 90)$ ground-truth matrix, where 360 and 90 correspond to azimuth and elevation angles, respectively, each with one-degree resolution [27]. Each matrix entry represents a single real-valued signal power for its corresponding direction. The loss function \mathcal{L} combines the \mathcal{L}_1 loss and the Structural

Table 1: Hyperparameter settings.

Symbol	Meaning	Value
ϵ_μ	Threshold for mean gradient	0.0002
ϵ_r	Threshold for radius	10.0
ϵ_ρ	Threshold for attenuation	0.004
N_μ	Gradient check frequency	100
N_ρ	Attenuation check frequency	100
r_{rx}	Radius of the RESS	1.0
ϕ	Scaling matrix reduction factor	1.6
λ	Balance two losses	0.2

Similarity Index Measure (\mathcal{L}_{SSIM}) loss:

$$\mathcal{L} = (1 - \lambda)\mathcal{L}_1 + \lambda\mathcal{L}_{SSIM} \quad (8)$$

where \mathcal{L}_1 measures the average difference between the actual and predicted signal power across all rays. Since the (360, 90) matrix can be viewed as an image (Figure 6), \mathcal{L}_{SSIM} evaluates the structural similarity between the predicted and ground-truth "images," helping *RFSPM* learn spatial patterns across rays. The parameter λ balances these two losses.

ii) Single Antenna: For a single antenna, the ground-truth received signal is either a single real-valued signal power or a complex-valued number containing both amplitude and phase, assumed to be the sum of signals from all directions [27]. Thus, *RFSPM* computes the predicted signal by summing the signals from all rays. If the received signal is real-valued, the \mathcal{L}_1 loss is applied. For a complex-valued signal, the \mathcal{L}_1 loss is computed separately for amplitude and phase, then averaged to obtain the final loss.

6 Implementation

Training: Table 1 presents the hyperparameter settings, defined in Section 5. These values are determined through extensive empirical studies. The attributes of all 3D Gaussians are updated using SGD [34]. The learning rates are set as follows: $\eta_\rho = 0.01$ for attenuation, $\eta_\psi = 0.0025$ for emission, $\eta_s = 0.01$ for the scaling matrix, and $\eta_R = 0.005$ for the rotation matrix. The learning rate for the mean, η_μ , starts at 0.00016 and decreases exponentially to 1.6×10^{-6} over 30,000 iterations. For Gaussian count optimization, the number of Gaussians is optimized only during the first half of the total iterations. After that, only the attributes of the Gaussians are updated.

CUDA Kernel: Each grid contains 16 rays in both azimuth and elevation angles, totaling $N_{rays} = 16 \times 16$ rays per grid. Gaussians intersecting each grid are sorted using the CUDA built-in `cub::DeviceRadixSort` API [52]. Each splatting instance (a Gaussian intersecting a grid) is assigned a 64-bit key: the lower 32 bits store the distance to the receiver, while the upper 32 bits encode the grid index. This structure

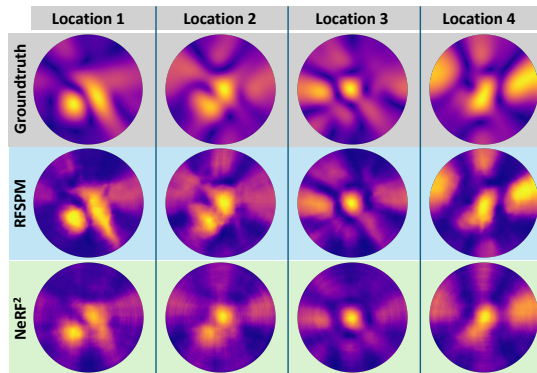


Figure 6: NeRF² and RFSPM visualizations of spatial spectrum at four transmitter positions.

enables efficient parallel sorting of all splats by distance with a single invocation of the `cub::DeviceRadixSort` API.

To integrate PyTorch with CUDA execution, we implement a custom PyTorch extension using C++ and CUDA, enabling efficient GPU-accelerated computations. The forward and backward computations are encapsulated within a subclass of `torch.autograd.Function`, ensuring seamless differentiation and gradient propagation within PyTorch’s computational graph. The Python interface, implemented via PyTorch’s C++ API, facilitates interaction between PyTorch tensors and CUDA kernels, handling memory layout conversions and efficient CPU-GPU data transfers.

7 Evaluation

We evaluate *RFSPM* in three studies and two applications:

- **RFID** spatial spectrum synthesis;
- **BLE** received signal strength indicator (RSSI) prediction, applied to fingerprinting-based localization application;
- **LoRa** RSSI prediction, applied to LoRa gateway coverage estimation application.

7.1 Field Study - RFID Spectrum Synthesis

7.1.1 Experimental Setup. i) TASK: Given a transmitter sending signals at location (x_{tx}, y_{tx}, z_{tx}) , the task is to synthesize the spatial spectrum received by the receiver (antenna array) at a fixed location. The spatial spectrum, represented as a (360, 90) matrix, captures received signal power from all directions, covering azimuth and elevation angles at one-degree resolution. The elevation angle is limited to 90° as only the front hemisphere of the antenna array is considered [27].

ii) DATASET: The public RFID dataset from NeRF² [27], collected in real-world environments, is employed. It contains 6,123 transmitter (RFID tag) locations within a 3D space of 275.8 ft^3 and their corresponding spatial spectra, received by a receiver with a 4×4 antenna array operating at 915 MHz. The dataset is randomly split 70% training and 30% testing.

iii) METRICS: We employ the following two metrics:

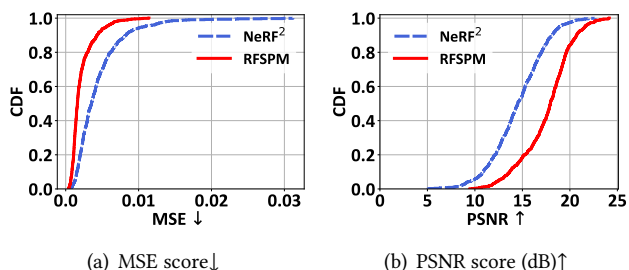


Figure 7: Comparison between NeRF² and RFSPM for sparse measurement density of 0.8 measurements/ft³.

- Mean Squared Error (MSE)↓: This metric calculates the average of the squared differences between the synthesized spectrum and the ground truth.
- Peak Signal-to-Noise Ratio (PSNR, in dB)↑: Treating the spatial spectrum as an image, PSNR measures structural similarity, with higher values indicating better quality.

IV) BASELINES: We compare RFSPM with NeRF² [27]. Other simulation-based or ML-based methods, such as simulation via MATLAB [20], DCGAN [53], and VAE [25], perform worse on the RFID dataset [27] compared to NeRF².

7.1.2 Overall Performance. Setting: To evaluate RFSPM’s performance in scenarios with insufficient data, we randomly select 220 instances from the training dataset instead of using the full training data. This creates a sparse dataset with a measurement density of 0.8 measurements/ft³.

Result: Figure 6 presents the real-collected spatial spectra for four randomly selected transmitter positions (first row), alongside those generated by RFSPM (second row) and NeRF² (third row). Visually, the spectra synthesized by RFSPM more closely match the ground truth compared to those by NeRF². Figure 7 then shows the Cumulative Distribution Function (CDF) of the two metric scores for both models on the testing data. RFSPM outperforms NeRF² by 21.2% and 56.4% on average in PSNR and MSE, respectively. This superior performance is attributed to the Gaussian-based scene representation module, which enables more efficient learning of scene representation from sparse training data.

7.1.3 Training and Inference Time. Setting: Both methods are trained for 100,000 iterations. Training time is measured by running each method 10 times on two computers equipped with NVIDIA GeForce RTX 3080 Ti or 4090 GPUs. Inference time for each model is also recorded.

Result: Figure 8 shows that RFSPM trains in 0.27 hours, achieving an 18.56-fold speedup over NeRF²’s 5.01 hours. Similarly, Figure 9 demonstrates that RFSPM achieves an 84.39-fold speedup, reducing inference time from 352.73 ms with NeRF² to 4.18 ms with RFSPM. This improvement is due to the flexible Gaussian-based scene representation, which avoids computations in empty space and focuses only on

areas containing objects. Moreover, RFSPM’s ray tracing algorithm avoids querying large MLP networks, a significant time-consuming process in NeRF².

7.1.4 Measurement Density. Setting: We compare the performance of RFSPM (trained on a dataset with a density of 0.8 measurements/ft³) to NeRF² (trained on varying densities: 0.8, 1.6, 3.1, 4.7, 7.8, 12.4, and 15.5 measurements/ft³).

Result: Figure 10 presents the MSE scores on the testing dataset. RFSPM achieves a comparable MSE to NeRF² trained on a dataset with a density of 7.8 measurements/ft³. Specifically, RFSPM records an average MSE of 0.0312, compared to 0.0349 for NeRF². This indicates that RFSPM requires 9.8 × less training data to achieve similar spectrum quality to NeRF². The improvement arises from RFSPM’s 3D Gaussian-based scene representation, which focuses on object features rather than empty space, making it more efficient than NeRF²’s voxel-based radiance fields.

7.1.5 Practical Benefits. An angular artificial neural network (AANN) identifies the Angle of Arrival (AoA) of line-of-sight path from received spatial spectra, enabling spectrum-based localization [54]. The AANN is trained on pairs of spectra and their corresponding AoA labels. Both RFSPM and NeRF² can synthesize spectra for AANN training.

Compared to NeRF², adopting RFSPM can significantly reduce real-world resource consumption. For example, in a conference room (26.2 ft × 16.4 ft × 9.8 ft) [35] with a measurement time of one minute per measurement, reducing the measurement density from 7.8 to 0.8 measurements/ft³ saves approximately 200 hours of data collection time. Additionally, RFSPM reduces computing time by 5.71 hours, including 4.74 hours for training and 0.97 hours for inference, both of which greatly save computational resources. Localization results with an AANN trained on synthesized spectra are not presented in this section. However, as shown in Section 7.1.2, RFSPM’s superior spectrum quality suggests improved localization performance. Section 7.2 further quantifies the localization-related performance gain.

7.2 Field Study - BLE RSSI Prediction

7.2.1 Experimental Setup. 1) TASK: This task verifies that RFSPM supports single-antenna setups capturing a single-valued RSSI. Given a transmitter (BLE node) sending signals from location (x_{tx}, y_{tx}, z_{tx}) , the goal is to predict the RSSI (in dBm) received by a receiver (BLE gateway with a single antenna) at a fixed location. The measured RSSI represents the aggregate signal power from all directions [27].

Additionally, we conduct a fingerprint-based localization application to showcase RFSPM’s sensing advantages.

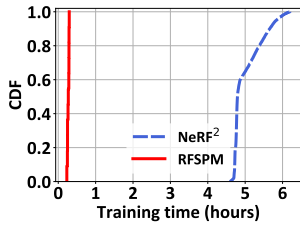


Figure 8: Training times for spectrum synthesis.

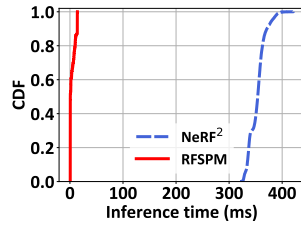


Figure 9: Inference times for spectrum synthesis.

II) DATASET: The public BLE dataset [27], collected in an elderly nursing home, is employed. Twenty-one receivers operating at 2.4 GHz capture RSSI readings. The dataset contains 6,000 transmitter positions, each paired with a 21-dimensional tuple of RSSI readings from the 21 receivers. If a receiver misses a signal, the RSSI is recorded as -100 dBm. The dataset is randomly split 70% training and 30% testing.

III) METRICS: RSSI prediction error is the absolute difference between the model’s predictions and the ground truth.

IV) BASELINES: We compare *RFSPM* with *NeRF²*. Other empirical and ML-based methods, including MRI [55] and CGAN [24], are excluded because they perform worse than *NeRF²* on the same testing dataset, as demonstrated in [27].

7.2.2 Overall Performance. **Setting:** To evaluate the performance of *RFSPM* in scenarios with sufficient data, both models are trained on the full training dataset.

Result: Figure 11 indicates that *RFSPM* achieves an average RSSI prediction error of 4.09 dBm, compared to *NeRF²*’s 6.09 dBm. This represents a 32.79% improvement, highlighting *RFSPM*’s effectiveness even with a single-antenna receiver. The performance gain stems from *RFSPM*’s flexible 3D Gaussian-based scene representation, which efficiently utilizes training data by focusing on objects rather than empty space and aligning with object geometry.

7.2.3 Localization Application. **Setting:** In fingerprinting-based localization, the RSSI value from an unknown transmitter queries a fingerprint database containing pairs of transmitter positions and corresponding RSSI values. The K Nearest Neighbors (KNN) identifies the K nearest matches and estimates the unknown transmitter position as the average of these K positions [24]. We generate synthetic datasets using *RFSPM* and *NeRF²*, trained as described in subsection 7.2.2, to build the fingerprint database for comparison.

Result: Figure 12 shows that *RFSPM* outperforms *NeRF²* by 31.40% on average. The slightly smaller localization gain compared to the RSSI prediction gain is due to the resilience of the KNN algorithm, which mitigates prediction errors by averaging across K nearest neighbors. This demonstrates that high-fidelity data benefits localization applications.

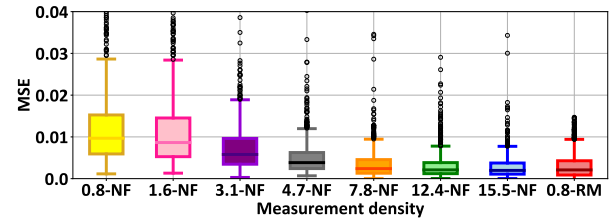


Figure 10: MSE of *RFSPM* (RM) at 0.8 measurements/ft³ and *NeRF²* (NF) across different densities.

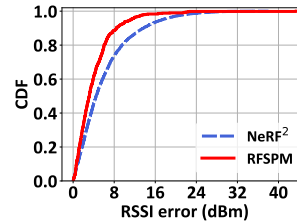


Figure 11: RSSI prediction errors on the BLE dataset.

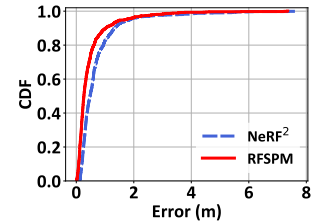


Figure 12: Fingerprinting-based localization error.

7.2.4 Practical Benefits. Similar to the previous field study, *RFSPM* eliminates the need for site surveys, significantly reducing data collection time. Its fast training GPU-hours and low inference latency save server computation resources, accelerating the construction of the fingerprint database.

7.3 Field Study - LoRa RSSI Prediction

7.3.1 Experimental Setup. I) TASK: Given a transmitter (LoRa node) at any location (x_{tx}, y_{tx}, z_{tx}) , the task is to predict the single-valued RSSI (in dBm) received by a fixed receiver (LoRa gateway with a single antenna).

Additionally, we conduct the LoRa gateway coverage estimation application to demonstrate the practical advantages of *RFSPM* for network planning task.

II) DATASET: We use LoRa network [56] to collect spatial dataset in a pistachio orchard [57], where trees have an average height of 6.0 m, are spaced 4.9 m apart in columns, and 6.6 m apart between rows. The receiver has a single antenna and reports a single-valued signal strength, RSSI, in dBm for each transmitter location. The transmitter is positioned at the right side of 64 trees in an 8×8 grid, with the average RSSI from 10 measurements at each location taken as the ground truth. Since this data alone is insufficient to train models, we augment it by adding Gaussian noise with a mean of zero and a standard deviation of 0.1 m to each transmitter location. The augmented locations are assigned the same RSSI values as the original transmitter locations, resulting in a total of 6,400 transmitter location measurements. The dataset is randomly split 70% training and 30% testing.

III) METRICS: RSSI prediction error is the absolute difference between the model’s predictions and the ground truth.

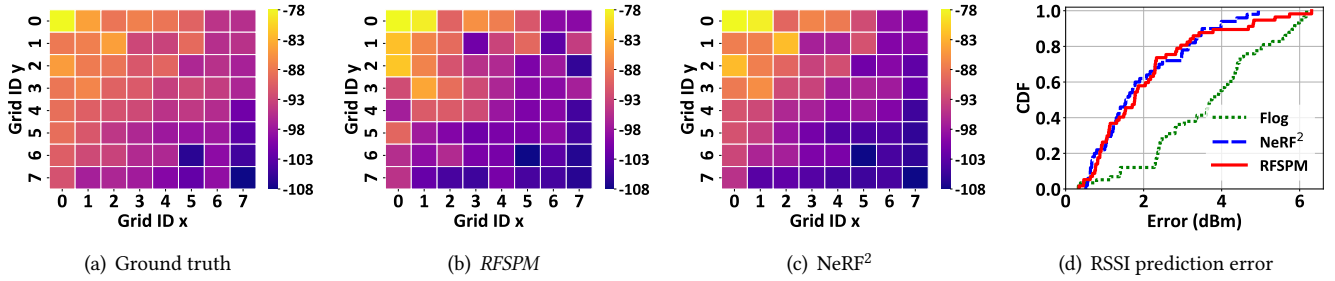


Figure 13: RSSI prediction from three methods (*RFSPM* uses only 30% of the training data; others use 100%).

IV) **BASELINES:** We compare *RFSPM* with NeRF² [27]. We also include FLog [58], a state-of-the-art empirical model for orchards built on the Log-Normal [21] model.

7.3.2 **Overall Performance. Setting:** To highlight *RFSPM*'s data efficiency, it is trained on only 30% of the full training data, *i.e.*, $6400 * 70% * 30% = 1344$. In contrast, baselines use the full training data, *i.e.*, $6400 * 70% = 4480$. All methods are evaluated on the same testing data.

Result: Figure 13 presents heatmaps of the ground truth and the generated RSSI from NeRF² and *RFSPM*, along with the CDF of RSSI prediction errors for all models. From Figures 13(a-c), *RFSPM* and NeRF² achieve similar generation accuracy, as verified in Figure 13(d). However, *RFSPM* uses at least $3\times$ less training data compared to NeRF², demonstrating its practical data efficiency. Figure 13(d) also shows that both *RFSPM* and NeRF² outperform the FLog model. This is because FLog oversimplifies complex RF signal propagation by relying on a single path loss exponent (PLE) [21], whereas *RFSPM* and NeRF² compute more fine-grained effects across the entire space through their scene representation modules.

7.3.3 **Gateway Coverage Estimation Application. Setting:** Generated RSSI data can estimate a receiver's coverage by calculating the Bit Error Rate (BER), using RSSI values and the Spreading Factor (SF) as inputs to the existing BER calculation equation [59]. A BER below 10^{-4} indicates sufficient reliability, with a packet delivery ratio exceeding 90% [60].

Result: Both theoretically calculated BER values, derived from *RFSPM*'s generated data, and measured BER values are effectively zero across all ranges, confirming reliable coverage. Leveraging *RFSPM*'s high fidelity, detailed coverage maps can be generated. Given the orchard's uniform layout, similar coverage maps can be assumed for all receivers, enabling strategic placement to ensure full coverage, minimize blind spots, and optimize resource allocation. These findings provide confidence in transceiver deployment, ensuring reliable data transmission for applications such as environmental monitoring in precision agriculture.

7.3.4 **Practical Benefits.** *RFSPM* provides several practical advantages, including cost savings by reducing the number of

gateways (up to 20,000 per gateway [61]), high-fidelity coverage maps to eliminate blind spots, and optimized resource allocation for maximum coverage with minimal hardware. It enables scalable deployment through customizable maps for vast orchards. Reliable connectivity supports precision agriculture technologies like soil monitoring and autonomous machinery, enhancing efficiency and sustainability while lowering energy consumption and environmental impact.

8 Conclusion and Future Work

This paper introduces *RFSPM* for scalable RF signal propagation modeling. We customize 3D Gaussian attributes and employ gradient-guided learning, integrating an RF-customized CUDA-based ray tracing module for efficient 3D scene representation and received signal computation. Extensive experiments validate *RFSPM*'s efficiency. Future work explores key challenges and potential enhancements.

Multiple Receivers in a Scene: Our system currently supports a single fixed receiver for predicting signals at any transmitter location in a scene. However, real-world scenarios may involve multiple receivers. Since they share the same physical space, a potential solution is a coordinate-based transformation function that models RF propagation variations with receiver location, allowing for interpolation and extrapolation of RF signal characteristics.

Generalizability Across Scenes: Our system enables quick training when data is available for each scene. However, it does not support zero-shot inference for new scenes. A potential solution is pre-training on large multi-scene datasets to enhance generalization, leveraging transfer learning for adaptation with minimal or no additional training.

Temporal Dynamics: Our system is designed for static environments. If the scene layout changes, retraining or fine-tuning is required. A potential solution is to incorporate recurrent learning mechanisms to capture temporal dependencies. For example, each Gaussian's attributes can be modeled as a function of discrete time steps, enabling the system to adapt to environmental changes.

Acknowledgments

This research was funded in part by the Air Force Office of Scientific Research under awards # FA95502210193 and FA95502310559, and the DEVCOM Army Research Laboratory under award # W911NF-17-2-0196. Wan Du was partially supported by NSF Grant # 2239458, a UC Merced Fall 2023 Climate Action Seed Competition grant, and a UC Merced Spring 2023 Climate Action Seed Competition grant. Kang Yang was partially supported at UC Merced by a financial assistance award approved by the Economic Development Administration's Farms Food Future program. Sijie Ji's research is supported through a Schmidt Science Fellowship.

References

- [1] Yongsan Ma, Gang Zhou, and Shuangquan Wang. WiFi sensing with channel state information: A survey. *ACM Computing Surveys*, 52(3):1–36, 2019.
- [2] Ali Abedi, Farzan Dehbashi, Mohammad Hossein Mazaheri, Omid Abari, and Tim Brecht. WiTAG: Seamless WiFi Backscatter Communication. In *ACM SIGCOMM*, 2020.
- [3] Ryu Okubo, Luke Jacobs, Jinhua Wang, Steven Bowers, and Elahe Soltanaghai. Integrated Two-way Radar Backscatter Communication and Sensing with Low-power IoT Tags. In *ACM SIGCOMM*, 2024.
- [4] Hang Zhu, Varun Gupta, Satyajeet Singh Ahuja, Yuandong Tian, Ying Zhang, and Xin Jin. Network planning with deep reinforcement learning. In *ACM SIGCOMM*, 2021.
- [5] Md Maruf Ahamed and Saleh Faruque. 5G network coverage planning and analysis of the deployment challenges. *Sensors*, 21(19):6608, 2021.
- [6] R Ivan Zelaya, William Sussman, Jeremy Gummeson, Kyle Jamieson, and Wenjun Hu. LAVA: fine-grained 3D indoor wireless coverage for small IoT devices. In *ACM SIGCOMM*, 2021.
- [7] Enes Krijestorac, Samer Hanna, and Danijela Cabric. Spatial Signal Strength Prediction using 3D Maps and Deep Learning. In *IEEE ICC*, 2021.
- [8] Xianzhong Ding, Alberto Cerpa, and Wan Du. Exploring deep reinforcement learning for holistic smart building control. *ACM Transactions on Sensor Networks*, 20(3):1–28, 2024.
- [9] Xianzhong Ding, Alberto Cerpa, and Wan Du. Multi-zone hvac control with model-based deep reinforcement learning. *IEEE Transactions on Automation Science and Engineering*, 2024.
- [10] Roshan Ayyalasomayajula, Aditya Arun, Chenfeng Wu, Sanatan Sharma, Abhishek Rajkumar Sethi, Deepak Vasishth, and Dinesh Bhargava. Deep Learning based Wireless Localization for Indoor Navigation. In *ACM MobiCom*, 2020.
- [11] Haofan Lu, Mohammad Mazaheri, Reza Rezvani, and Omid Abari. A Millimeter Wave Backscatter Network for Two-Way Communication and Localization. In *ACM SIGCOMM*, 2023.
- [12] Kang Yang, Yuning Chen, and Wan Du. OrchLoc: In-Orchard Localization via a Single LoRa Gateway and Generative Diffusion Model-based Fingerprinting. In *Proceedings of the 22nd ACM International Conference on Mobile Systems, Applications, and Services (MobiSys)*, 2024.
- [13] Pushpendu Kar and Bhasker Dappuri. Site Survey and Radio Frequency Planning for the Deployment of Next Generation WLAN. In *IEEE WiSPNET*, 2018.
- [14] Cisco. Understand Site Survey Guidelines for WLAN Deployment. <https://www.cisco.com/c/en/us/support/docs/wireless/5500-series-wireless-controllers/116057-site-survey-guidelines-wlan-00.html>, 2023. [Online].
- [15] R.G. Kouyoumjian and P.H. Pathak. A Unifim Geometrical Theory of Diffraction for an Edge in a Perfectly Conducting Surface. *Proceedings of the IEEE*, 62(11):1448–1461, 1974.
- [16] Han Na and Thomas F Eibert. A Huygens' Principle Based Ray Tracing Method for Diffraction Calculation. In *IEEE EuCAP*, 2022.
- [17] James Clerk Maxwell. *A Treatise on Electricity and Magnetism*, volume 1. Oxford: Clarendon Press, 1873.
- [18] REMCOM. Wireless InSite. <https://www.remcom.com/wireless-insite-propagation-software>, 2024. [Online].
- [19] Tribhuvanesh Orekondy, Pratik Kumar, Shreya Kadambi, Hao Ye, Joseph Soriaga, and Arash Behboodi. WiNeRT: Towards Neural Ray Tracing for Wireless Channel Modelling and Differentiable Simulations. In *ICLR*, 2023.
- [20] MATLAB. RayTracing Toolbox. <https://www.mathworks.com/help/antenna/ref/rfprop.raytracing.html>, 2024. [Online].
- [21] Theodore S Rappaport et al. *Wireless Communications: Principles and Practice*, volume 2. prentice hall PTR New Jersey, 1996.
- [22] John David Parsons. *Mobile Communication Systems*. Springer Science & Business Media, 2012.
- [23] Masaharu Hata. Empirical Formula for Propagation Loss in Land Mobile Radio Services. *IEEE transactions on Vehicular Technology*, 29(3):317–325, 1980.
- [24] Felipe Parralejo, Fernando J Aranda, José A Paredes, Fernando J Alvarez, and Jorge Morera. Comparative Study of Different BLE Fingerprint Reconstruction Techniques. In *IEEE IPIN*, 2021.
- [25] Zikun Liu, Gagandeep Singh, Chenren Xu, and Deepak Vasishth. FIRE: enabling reciprocity for FDD MIMO systems. In *ACM MobiCom*, pages 628–641, 2021.
- [26] Mehrzad Malmirchegini and Yasamin Mostofi. On the Spatial Predictability of Communication Channels. *IEEE Transactions on Wireless Communications*, 11(3):964–978, 2012.
- [27] Xiaopeng Zhao, Zhenlin An, Qingrui Pan, and Lei Yang. NeRF²: Neural Radio-Frequency Radiance Fields. In *ACM MobiCom*, 2023.
- [28] Ben Mildenhall, Pratul P Srinivasan, Matthew Tancik, Jonathan T Barron, Ravi Ramamoorthi, and Ren Ng. NeRF: Representing Scenes as Neural Radiance Fields for View Synthesis. In *ECCV*, 2020.
- [29] Bernhard Kerbl, Georgios Kopanas, Thomas Leimkühler, and George Drettakis. 3D Gaussian Splatting for Real-Time Radiance Field Rendering. In *SIGGRAPH*, 2023.
- [30] Volker Schönefeld. Spherical harmonics. *Computer Graphics and Multimedia Group, Technical Note. RWTH Aachen University, Germany*, 18, 2005.
- [31] Arne Schmitz, Thomas Karolski, and Leif Kobbelt. Using Spherical Harmonics for Modeling Antenna Patterns. In *IEEE Radio and Wireless Symposium*. IEEE, 2012.
- [32] Noah Snavely, Steven M Seitz, and Richard Szeliski. Photo Tourism: Exploring Photo Collections in 3D. In *ACM SIGGRAPH*, 2006.
- [33] NVIDIA. CUDA Programming Guide. <https://docs.nvidia.com/cuda/cuda-c-programming-guide/index.html>, 2024. [Online].
- [34] Shun-ichi Amari. Backpropagation and stochastic gradient descent method. *Neurocomputing*, 5(4-5):185–196, 1993.
- [35] MATLAB. Three-Dimensional Indoor Positioning with 802.11az Fingerprinting and Deep Learning. <https://www.mathworks.com/help/wlan/ug/three-dimensional-indoor-positioning-with-802-11az-fingerprinting-and-deep-learning.html>, 2024. [Online].
- [36] Thomas L Marzetta, Erik G Larsson, and Hong Yang. *Fundamentals of massive MIMO*. Cambridge University Press, 2016.
- [37] Haofan Lu, Christopher Vatheuer, Baharan Mirzasoileiman, and Omid Abari. NeWRF: A Deep Learning Framework for Wireless Radiation Field Reconstruction and Channel Prediction. In *ICML*, 2024.
- [38] Song Han, Jeff Pool, John Tran, and William Dally. Learning both Weights and Connections for Efficient Neural Networks. In *NeurIPS*,

- 2015.
- [39] Cheng-Yu Hsieh, Chun-Liang Li, Chih-Kuan Yeh, Hootan Nakhost, Yasuhisa Fujii, Alexander Ratner, Ranjay Krishna, Chen-Yu Lee, and Tomas Pfister. Distilling Step-by-Step! Outperforming Larger Language Models with Less Training Data and Smaller Model Sizes. *arXiv preprint arXiv:2305.02301*, 2023.
- [40] Tero Karras, Miika Aittala, Janne Hellsten, Samuli Laine, Jaakko Lehtinen, and Timo Aila. Training Generative Adversarial Networks with Limited Data. In *NeurIPS*, 2020.
- [41] Gaurav Menghani. Efficient Deep Learning: A Survey on Making Deep Learning Models Smaller, Faster, and Better. *ACM Computing Surveys*, 55(12):1–37, 2023.
- [42] Yucheng Yin, Zinan Lin, Minhao Jin, Giulia Fanti, and Vyas Sekar. Practical GAN-based Synthetic IP Header Trace Generation using NetShare. In *ACM SIGCOMM*, 2022.
- [43] Daniel Neil, Michael Pfeiffer, and Shih-Chii Liu. Learning to be Efficient: Algorithms for Training Low-Latency, Low-Compute Deep Spiking Neural Networks. In *ACM SAC*, 2016.
- [44] Zili Liu, Tu Zheng, Guodong Xu, Zheng Yang, Haifeng Liu, and Deng Cai. Training-Time-Friendly Network for Real-Time Object Detection. In *AAAI*, 2020.
- [45] Priya Goyal, Piotr Dollár, Ross Girshick, Pieter Noordhuis, Lukasz Wesolowski, Aapo Kyrola, Andrew Tulloch, Yangqing Jia, and Kaiming He. Accurate, Large Minibatch SGD: Training ImageNet in 1 Hour. *arXiv preprint arXiv:1706.02677*, 2017.
- [46] Yao Fu, Leyang Xue, Yeqi Huang, Andrei-Octavian Brabete, Dmitrii Ustiugov, Yuvraj Patel, and Luo Mai. ServerlessLLM: Low-Latency Serverless Inference for Large Language Models. In *USENIX OSDI*, 2024.
- [47] Tao Wang, Tuo Shi, Xiulong Liu, Jianping Wang, Bin Liu, Yingshu Li, and Yechao She. Minimizing Latency for Multi-DNN Inference on Resource-Limited CPU-Only Edge Devices. In *IEEE INFOCOM*, 2024.
- [48] Shuai Zhang, Sheng Zhang, Zhuzhong Qian, Jie Wu, Yibo Jin, and Sanglu Lu. DeepSlicing: Collaborative and Adaptive CNN Inference With Low Latency. *IEEE Transactions on Parallel and Distributed Systems*, 32(9):2175–2187, 2021.
- [49] Max Born and Emil Wolf. *Principles of Optics*. Cambridge University Press, 2013.
- [50] Sandra De Iaco, DE Myers, and Donato Posa. Strict Positive Definiteness of a Product of Covariance Functions. *Communications in Statistics-Theory and Methods*, 40(24):4400–4408, 2011.
- [51] Towaki Takikawa, Joey Litalien, Kangxue Yin, Karsten Kreis, Charles Loop, Derek Nowrouzezahrai, Alec Jacobson, Morgan McGuire, and Sanja Fidler. Neural Geometric Level of Detail: Real-time Rendering with Implicit 3D Shapes. In *IEEE/CVF CVPR*, 2021.
- [52] NVIDIA. Device-Wide Primitives. https://nvidia.github.io/cccl/cub/device_wide.html, 2024. [Online].
- [53] Alec Radford, Luke Metz, and Soumith Chintala. Unsupervised Representation Learning with Deep Convolutional Generative Adversarial Networks. *arXiv preprint arXiv:1511.06434*, 2015.
- [54] Zhenlin An, Qiongzhen Lin, Ping Li, and Lei Yang. General-Purpose Deep Tracking Platform across Protocols for the Internet of Things. In *ACM MobiSys*, 2020.
- [55] Hyojeong Shin, Yohan Chon, Yungeun Kim, and Hojung Cha. MRI: Model-Based Radio Interpolation for Indoor War-Walking. *IEEE Transactions on Mobile Computing*, 14(6):1231–1244, 2014.
- [56] Muhammad Osama Shahid, Millan Philipose, Krishna Chintalapudi, Suman Banerjee, and Bhuvana Krishnaswamy. Concurrent interference cancellation: Decoding multi-packet collisions in LoRa. In *ACM SIGCOMM*, 2021.
- [57] Xianzhong Ding and Wan Du. Optimizing irrigation efficiency using deep reinforcement learning in the field. *ACM Transactions on Sensor Networks*, 20(4):1–34, 2024.
- [58] Kang Yang, Yuning Chen, Xuanren Chen, and Wan Du. Link Quality Modeling for LoRa Networks in Orchards. In *ACM/IEEE IPSN*, 2023.
- [59] Tallal Elshabrawy and Joerg Robert. Closed-form approximation of LoRa modulation BER performance. *IEEE Communications Letters*, 22(9):1778–1781, 2018.
- [60] Srikar Kasi and Kyle Jamieson. Towards quantum belief propagation for LDPC decoding in wireless networks. In *ACM MobiCom*, 2020.
- [61] Adam Simmons. How Much Does it Cost to Build a Cell Tower? <https://dgtlinfra.com/how-much-does-it-cost-to-build-a-cell-tower>, 2024. [Online].